Modeling High-Grade Serous Ovarian Carcinoma Using a Combination of *In Vivo* Fallopian Tube Electroporation and CRISPR-Cas9–Mediated Genome Editing

Katie Teng[1,2], Matthew J. Ford[1,2], Keerthana Harwalkar[1,2], YuQi Li[1,2], Alain S. Pacis[3], David Farnell[4,5], Nobuko Yamanaka[1], Yu-Chang Wang[2,6], Dunarel Badescu[2,6], Tuyet Nhung Ton Nu[7], Jiannis Ragoussis[2,6,8], David G. Huntsman[4,5], Jocelyne Arseneau[7], and Yojiro Yamanaka[1,2]

ABSTRACT

Ovarian cancer is the most lethal gynecologic cancer to date. High-grade serous ovarian carcinoma (HGSOC) accounts for most ovarian cancer cases, and it is most frequently diagnosed at advanced stages. Here, we developed a novel strategy to generate somatic ovarian cancer mouse models using a combination of *in vivo* electroporation and CRISPR-Cas9–mediated genome editing. Mutation of tumor suppressor genes associated with HGSOC in two different combinations (*Brca1, Tp53, Pten* with and without *Lkb1)* resulted in successfully generation of HGSOC, albeit with different latencies and pathophysiology. Implementing Cre lineage tracing in this system enabled visualization of peritoneal micrometastases in an immune-competent environment. In addition, these models displayed copy number alterations and phenotypes similar to human HGSOC. Because this strategy is flexible in selecting mutation combinations and targeting areas, it could prove highly useful for generating mouse models to advance the understanding and treatment of ovarian cancer.

Significance: This study unveils a new strategy to generate genetic mouse models of ovarian cancer with high flexibility in selecting mutation combinations and targeting areas.

Introduction

According to the American Cancer Society, 21,410 women in the United States will be newly diagnosed with ovarian cancer in 2021 and 13,770 will succumb to this devastating disease (1). It is ranked fifth in cancer deaths among women and is considered the most lethal gynecologic disease (1). High-grade serous ovarian carcinoma (HGSOC) is the most common type of ovarian cancer and is the cause of approximately 70% to 80% of all ovarian cancer deaths (2, 3). Because of the asymptomatic nature of this cancer, the majority of these patients are diagnosed at advanced stages (III or IV) after metastasis to the peritoneal cavity has occurred (3, 4).

Despite its name, the origin for HGSOC remains controversial (5, 6). The ovarian surface epithelium (OSE) has been the presumed cell-of-origin for HGSOC for many years (7). However, over recent years, the notion that the cell-of-origin for HGSOC resides in the OSE was challenged by the absence of a clearly defined precursor lesion in both the ovary and OSE in patients (8). High-risk patients, such as *BRCA1* and *BRCA2* mutation carriers, often undergo prophylactic salpingo-oophorectomies in which both their fallopian tubes (FT) and ovaries are removed (9, 10). Interestingly, by extensively examining the distal end of these FTs using the "sectioning and extensively examining the fimbriated end" (SEE-FIM) protocol, microscopic precancerous lesions such as serous tubal intraepithelial carcinomas (STIC) were identified (11–13). Genomic studies have revealed that these precursor lesions carry the same mutations as the HGSOC tumors that form. These data suggests the distal fallopian tube epithelium (FTE) can be a cell-of-origin for HGSOC (11, 14, 15). However, in sporadic cases of HGSOC, STICs are only identified in 50% to 60% of patients, while the remaining 40% to 50% are undetectable (8). It is unknown whether this is simply due to inaccurate detection or if there is another source for HGSOC tumorigenesis (16, 17). "Precursor escape" has been a proposed hypothesis to explain the lack of STICs in some patients with widespread HGSOC (14, 18). This theory proposes that small early serous proliferations in the fallopian tube escape and can give rise to HGSOC without forming identifiable STICs (14, 18); however, further studies still need to be performed to validate this theory.

HGSOC tumors display significant genomic heterogeneity and are driven by copy number alterations as few somatic mutations are detected in the tumors (8, 19). The most common recurrent mutation detected are *TP53* mutations found in 96% of the tumors while mutations or silencing in *BRCA* genes and other homologous recombination repair genes account for a total of 50% of HGSOC cases (8, 19). In addition, several distinct copy number signatures have been identified that are linked to molecular pathways and drug responsiveness (20, 21), suggesting that the multi-mutational processes in single HGSOC patients contribute to the complex evolution of HGSOC subtypes. Although recurrent amplification and deletion of chromosomal loci have been reported in several articles (21–24), the genes and pathways driving cell proliferation and metastasis have not been fully explored. Alterations of single chromosomal loci affect hundreds of

[1]Rosalind and Morris Goodman Cancer Research Centre, McGill University, Montreal, Canada. [2]Department of Human Genetics, McGill University, Montreal, Canada. [3]Canadian Centre for Computational Genomics, McGill University, Montreal, Canada. [4]Department of Pathology, Laboratory Medicine, University of British Columbia, Vancouver, British Columbia. [5]Department of Molecular Oncology, BC Cancer Research Institute, Vancouver, British Columbia. [6]McGill University and Genome Centre, Montreal, Canada. [7]Department of Pathology, McGill University Hospital Research Institute, Montreal, Canada. [8]Department of Bioengineering, McGill University, Montreal, Canada.

Note: Supplementary data for this article are available at Cancer Research Online (http://cancerres.aacrjournals.org/).

Corresponding Author: Yojiro Yamanaka, Rosalind and Morris Goodman Cancer Research Centre, Human Genetics, McGill University, 1160 Pine Avenue West, rm419, Montreal, Quebec H3A1A3, Canada. Phone: 514-398-8776; E-mail: yojiro.yamanaka@mcgill.ca

Cancer Res 2021;81:5147–60

doi: 10.1158/0008-5472.CAN-20-1518

genes, and currently, there has not been an effective strategy to identify the genes important for driving tumorigenesis and pathophysiology of HGSOCs.

Developing genetically engineered mouse models (GEMM) have proven to be effective in understanding cancer initiation and progression (25). These models allow for the study of gene function *in vivo* and elucidate the pathways involved in early tumorigenesis (25). However, traditional germline GEMMs are limited by availability of lineage specific Cre mouse lines and conditional alleles of the gene-of-interest. In addition, generation of desired genetic combinations in germline GEMMs is costly and can be time-consuming. In ovarian cancer modeling, *Pax8-TetOn-Cre* and *Ovgp1-CreERT2* systems were used successfully to generate HGSOCs from the FTE; however, these systems would not be suitable to examine various allelic combinations and screening for other candidate genes involved in HGSOC tumorigenesis.

Here, we present an *in vivo* electroporation method that can be used to target the distal murine fallopian tube and ovarian surface epithelium with high flexibility in selecting gene targets. CRISPR/Cas9 and Cre plasmids were directly injected into the fallopian tube lumen and were delivered via electroporation. By using this method, we successfully generated a model for HGSOC by targeting *Brca1, Tp53*, and *Pten* and showed that with the addition of *Lkb1* loss, the cell-of-origin can vary and significantly decrease tumor latency while increasing penetrance. This indicates the cell type-specific susceptibilities to malignant transformation and the subsequent link between cell-of-origin, combination of gene mutations, and pathophysiology of HGSOCs. In addition, by combining Cre-mediated lineage tracing, we were able to visualize peritoneal micrometastasis, which can be advantageous in studying the complex interaction between host and tumor cells during peritoneal implantation of HGSOC. The system developed has the potential to be a flexible and powerful tool for understanding malignancies arising from the female reproductive system in an immune competent environment.

Materials and Methods

Mouse lines

All mice were maintained in the Comparative Medicine and Animal Resources Centre at McGill University (Montreal, Canada). All the animal experiments were performed in accordance with institutional guidelines and were approved by the Facility Animal Care Committee (AUP #7843). Conditional *Lkb1*$^{flox/flox}$ mice (26) were obtained from the National Cancer Institute (Frederick, MD) and were maintained on a C57BL/6 background. Gt(ROSA)26Sor$^{tm14(CAG-tdTomato)Hze}$/J (27) mice were obtained from The Jackson Laboratory and crossed with *Lkb1*$^{flox/flox}$ mice to generate *Lkb1*$^{flox/flox}$; *Rosa-LSLtdTomato* mice.

In vivo oviductal electroporation

All the animal experiments were performed in accordance with institutional guidelines and were approved by the Facility Animal Care Committee (AUP #7843). The surgical procedure was adopted and modified from Takahashi and colleagues (28). A dorsal midline skin incision (1 cm) was performed and the female reproductive tract (oviduct/ovary) was exposed. Injection procedure was performed under a dissecting scope. Injection solution (approx. 1 μL) contained various plasmids (100–400 ng/μL each) and 0.05% of trypan blue, which was used as a marker for successful injection, was injected into the oviductal lumen using an air-pressure syringe system attached to a micromanipulator. Target region was covered with a small piece of PBS-soaked kimwipe and electroporated with 3 mm tweezer type electrodes (BTX Item #45–0487) connected to the BTX 830. Parameters: 30 V, 3 pulses, 1-second interval, P. length = 50 ms, unipolar. Following electroporation, the oviduct/ovary were placed back into their original position and the incisions were sutured.

Plasmids

PCS2 CreNLS plasmid (29) and PX330 plasmid (Addgene # 42230) were used in this study. CRISPR guide sequences (two guides/gene) were designed using ChopChop, CRISPR MIT, and Sequence Scan. Each guide efficiency was tested *in vitro* (Takara protocol) and *in vivo*. *Tp53* (#2, Exon 5) CATCGGAGCAGCGCTCATGG **TGG**, *Tp53* (#3, Exon 5) CGGAGCAGCGCTCATGGTGG **GGG**, *Pten* (#2, Exon 5) TGTGCATATTTATTGCATCG **GGG**, *Pten* (#3, Exon 7) AGCTGGCAGACCACAAACTG **AGG**, *Brca1* (#1, Exon 6) GCGTCGATCATCCAGAGCGT **GGG**, *Brca1* (#2, Exon 6) GCTACCGGAACCGTGTCAGA **AGG**.

Mouse dissection protocol

Mice were euthanized in accordance with institutional guidelines and were approved by the Facility Animal Care Committee (AUP #7843). If abdominal ascites was present, the fluid was collected with a 5ml syringe. Surgical scissors were used to cut the parietal peritoneum open and contents of the abdominal cavity were exposed. Images of the peritoneal cavity were taken under a fluorescent dissecting scope and RFP^{+} tumor samples were carefully dissected out. Each tumor sample (∼4 to 8 mm in diameter) was collected for histologic and molecular analysis.

Histopathology, immunohistochemistry, and immunofluorescence

Mouse tissue was fixed in 4% PFA at 4°C O/N and embedded in paraffin. Hematoxylin and eosin (H&E) staining was performed by the GCRC Histology Core Facility using 5-μm sections. Immunofluorescence staining was done using 5-μm sections. Antigen retrieval was performed in Tris/EDTA buffer for 7 minutes in pressure cooker. Blocking was done with 1% fish skin gelatin for 1 to 2 hours at room temperature in a humidified chamber. Primary staining was performed at 4°C O/N. Primary antibodies used: PAX8 (ProteinTech 10336–1-AP), Ki67 (Invitrogen, 14–5698–82), WT1 (Abcam, ab89901), CK8 (Abcam ab53280), acetylated tubulin (Sigma, T7451), phospho-AKT (Cell Signaling Technology, #4060), GATA4 (Invitrogen, #14–9980–82), and LYVE1 (ReliaTech, #103-PA50AG). Secondary staining was performed at room temperature for 1 to 2 hours. Secondary antibodies used: AF-488 phalloidin (Life Technologies, A12379), AF-635 phalloidin (Life Technologies, A34054), anti-Rabbit 488 (Invitrogen, A21206), anti-Rat 488 (Invitrogen, A21208), and anti-Mouse 488 (Invitrogen, A21202). Phalloidin and DAPI staining was performed during secondary staining period.

Confocal microscopy

Tissue sections and whole-mounts were mounted in ProLong Gold (Invitrogen, P10144) with a coverslip and were imaged using a Zeiss LSM800 microscope. Laser power thresholds were adjusted manually to give optimal fluorescence intensity for GFP, RFP, Far Red, and UV for each antibody combination and applied to each image.

MiSeq genotyping

MiSeq primers were ordered with CS1 and CS2 tags attached:

CS1 + Forward primer: 5′- ACACTGACGACATGGTTCTACA + specific forward primer -3′. CS2 + Reverse primer: 5′- TACGGTAGCAGAGACTTGGTCT + specific reverse primer -3′. The following

primers were used: *Brca1*-FOR 5′-TGCCCCTTTTTGTTTTACAGT-3′, *Brca1*-REV 5′-AGAACACTTGTCCAGCCACTA-3′(294bp); *Tp53*-FOR 5′-CTGTGCAGTTGTGGGTCAG-3′, *Tp53*-REV 5′-ACAAATTTCCTTCCACCCGG-3 (258bp); *Pten*(Ex5)-FOR 5′-GTTGCACAGTATCCTTTTGAAGA-3′, *Pten*(Ex5)-REV 5′-CAGCTTACCTTTTTGTCTCTGG-3′ (248bp); *Pten*(Ex7)-FOR 5′- AAGAAGTCCTTACATGGGTTGG-3′, *Pten*(Ex7)-REV 5′-TGGCTGAGGGAACTCAAAGT-3′ (290bp). Q5 polymerase was used for all PCR reactions. Initial denaturation at 98°C for 30 seconds, denatured at 98°C for 10 seconds, annealed/amplified at 67°C for 30 seconds, repeated 35×, final extension at 72°C for 2 minutes, and held at 4°C. Five microliters of PCR sample was run on a 2% agarose gel to visualize expected bands. Remaining PCR products were used for MiSeq amplicon sequencing (Illumina, Spike-in MiSeq PE 250bp) at the Génome Québec Innovation Centre at McGill University. All fastQ sequencing files with a minimum of 100 reads were analyzed using Cas-Analyzer (30) and 1% of the total number of reads were filtered out as sequencing errors.

Whole-genome sequencing of tumor samples

Whole-genome sequencing was performed on tumor samples #550912, #4450822, #600913, #50822, #500921, #760913, #40921, and #540822 to determine copy number alterations. Genomic DNA was isolated from freshly cut formalin-fixed paraffin-embedded sections using the GeneRead DNA FFPE Kit (Qiagen) followed by clean up with the Genomic DNA Clean & Concentrator Kit-10 (Zymo). Control DNA was isolated using an identical method from untargeted oviducts of the same mouse strain. Library preparation (Shotgun) and whole-genome sequencing was performed by Genome Quebec using the NovaSeq 6000 S4 PE150 (Illumina) to a depth of 35 M reads per sample.

Analysis of whole-genome sequencing

Raw reads were trimmed using Skewer (31) and the resulting reads were aligned to the GRCm38 mouse reference genome using BWA-MEM (32). Duplicates were marked using Picard (http://broadinstitute.github.io/picard/). Copy number variants (CNVs) were identified using CNVKit (33) at default parameters in each tumor sample and normal tissue as reference. Heatmaps were generated using CNVKit's heatmap command on all .cns segment files.

Isolation of cells from mouse ascites

A single-cell suspension was isolated from the ascites of mouse #50822. Ascites fluid was first incubated in RBC lysis buffer (Geneaid) for 5 minutes at room temperature followed by centrifugation for 5 minutes at 250 × *g*. The cell pellet was then resuspended in 500 μL of trypsin and incubated for 10 minutes at 37°C with agitation to singularize tumor cell aggregates. Media (500μL; DMEM/F12 (Gibco) with 10% v/v FBS) was added before centrifugation for 5 minutes at 250 × *g*. Pelleted cells were resuspended in media and passed through a 40-μm filter. The resulting single-cell suspension was used for scRNA-seq.

Quality control for scRNA-seq

An aliquot was taken from the cell suspension and incubated in live-dead staining consisting of working concentration of 2 μmol/L calcein-AM and 4 μmol/L Ethidium-Homodimer1 (Thermo Fisher Scientific L3224). After 10 minutes of incubation at room temperature, sample viability, concentration, segregation, size, and absence of large debris were verified by loading stained cell suspension onto hemocytometer (Incyto DHC-N01–5) and imaged on brightfield, GFP (for Calcein-AM) and RFP (for Ethidium homodimer-1) channels using a EVOS FL Auto Fluorescent microscope (Thermo Fisher Scientific). Percent viability is derived from GFP^+ cells (live cells) over the sum of GFP^+ plus RFP^+ cells (all cells) giving a viability score of 98%.

Generation of single-cell cDNA libraries and sequencing

The single-cell gene expression data were generated according to Chromium Single Cell 3′ Reagent Kits User Guide (v2 Chemistry, 10X genomics). Briefly, cells were suspended into Reverse Transcription (RT) Master Mix (10X genomics), then pipetted into Well-1 of a Chip "A" (10X genomics), followed by Gel Beads (10X genomics) into Well-2 and Partition oil (10X genomics) into Well-3. The chip assembly was run on a Chromium Controller (10X genomics), which generated Gel Bead-In-EMulsions (GEM). GEMs were pipetted out from the Chip and into a 200 μL PCR tube (Eppendorf 951010022) and ran on a thermocycler (Bio-Rad T100) with RT protocol [45 minutes at 53°C, 5 minutes at 85°C, hold at 4°C]. After RT, the GEMs content was released using Recovery Reagent (10X genomics) and cDNA were isolated using Buffer Sample Clean Up 1 (10X genomics) containing Silane Dynabeads (Thermo Fisher Scientific2000048). The purified cDNA was PCR amplified followed by purification using 0.6× volume SPRIselect beads (Beckman Coulter B23318). The cDNA quality (size distribution) and concentration were assessed using the LabChip (PerkinElmer 760517, CLS760672). A one-step fragmentation, end repair and A-tailing mix (10X genomics) were added to the cDNA in a 200 μL PCR tube and ran on a thermocycler with the protocol (hold at 4°C, 5 minutes at 32°C, 30 minutes at 65°C, hold at 4°C). The fragmented cDNA was subjected to double sided size selection using SPRIselect bead, by first suspending the fragmented cDNA in 0.6× volume of SPRIselect for 5 minutes, using 10x Magnetic Separator to pull down the beads, moving the suspension into another PCR tube and topped with 0.8× volume of SPRIselect. Following two rounds of 80% ethanol washes, the desired sized fragmented cDNA were eluted into adaptor ligation mix (10X genomics) and incubated for 15 minutes at 20°C. The ligated product was cleaned with 0.8× volume of SPRIselect, added to Sample Index PCR Mix (10X genomics), and amplified via 14 PCR cycles [45 seconds at 98°C (12 cycles of 20 seconds at 98°C, 30 seconds at 54°C, 20 seconds at 72°C), 1 minute at 72°C, hold at 4°C]. The final PCR product (or sequence ready library) was purified just like fragmented cDNA and quality controlled using LabChip as described earlier. Finally, the libraries were sequenced on Illumina Hiseq4000 PE100.

Analysis of single-cell RNA sequencing data

Raw sequencing data for each sample were converted to matrices of expression counts using the Cell Ranger software provided by 10X genomics (version 2.0.2). Briefly, raw BCL files from the Illumina HiSeq were demultiplexed into paired-end, gzip-compressed FASTQ files for each channel using Cell Ranger's mkfastq. Using Cell Ranger's count, reads were aligned to the mouse reference transcriptome (mm10) containing the *Tdtomato-WPRE-polyA* transcript, and transcript counts quantified for each annotated gene within every cell. The resulting UMI count matrix (genes × cells) were then provided as input to Seurat suite (version 2.3.4; ref. 34). Cells were first filtered to remove those that contain less than 200 genes detected and those in which >10% of the transcript counts were derived from mitochondrial-encoded genes. Clustering was performed using the "FindClusters" function and Uniform Manifold Approximation and Projection (UMAP) visualization for all cells. Cluster-specific gene markers were identified using Seurat's FindMarkers with cutoffs avg_logFC > 0.5 and FDR < 0.05. CNV analysis was performed using the inferCNV package (10.18129/B9.bioc.infercnv; ref. 35)

All sequence data were deposited to the Gene Expression Omnibus (GEO). The accession number is GSE179739.

Results

In vivo fallopian tube electroporation successfully delivered Cre and CRISPR plasmids into distal fallopian tube luminal epithelial cells for efficient genome manipulation

Development of the CRISPR/Cas9 system has permitted direct *in vivo* genome editing of somatic cells to generate GEMMs of cancer (24). Several somatic GEMMs of various types of cancers have been reported using different delivery methods, such as lenti- and adenoviral-mediated delivery for the lung, hydrodynamic delivery to the liver, and electroporation for the pancreas and developing brain (24). The advantage of these approaches is the minimum needed requirement of specific mouse lines and the flexibility in selecting gene mutation combinations and targeting locations.

To generate somatic GEMMs of ovarian cancer, we developed an *in vivo* fallopian tube electroporation method to deliver multiple DNA plasmids to the epithelium of the distal end of the fallopian tube (**Fig. 1A**). To test its delivery efficiency, a solution of Cre plasmid was directly injected into the lumen of the distal fallopian tube of 4- to 6-week-old *Rosa-LSLtdTomato* female mice. As a consequence of Cre excision, tdTomato (hereafter referred to as RFP)-positive cells were observed in the distal region of the fallopian tube (**Fig. 1B** and **E**). The RFP^+ cells were distributed stochastically throughout the luminal epithelium and targeted both $PAX8^+$ secretory and acetylated tubulin (AT)+ multiciliated cells, but not the stromal tissue compartment (**Fig. 1C** and **D**). In addition, a very small population of RFP^+ epithelial cells were also detected in the ovarian surface epithelium and hilum region (Supplementary Fig. S1).

To evaluate the effectiveness of our approach for HGSOC modeling, we targeted three tumor suppressor genes, *Brca1, Tp53*, and *Pten*, previously used to generate germline GEMMs of HGSOC using the *Pax8-TetOn-Cre* system (7). In addition to these three tumor suppressor genes, we selected an additional tumor suppressor gene, *LKB1* (also known as *STK11*). *LKB1/STK11* is an evolutionarily conserved pleiotropic kinase that regulates cell polarity, cell cycle, and energy metabolism and is deleted in many cancers (36, 37). Ch19p13.3, where the *LKB1* locus resides, is identified as one of many recurrent chromosomal deletions in HGSOC (19, 21). Somatic mutations in *LKB1* are not frequent; however, 90% of HGSOCs are significantly associated with either a shallow (monoallelic loss) or deep deletion in *LKB1* (**Fig. 1F**). In addition, downregulation of LKB1 protein is shown to be characteristic of HGSOC tumors, suggesting that loss-of-LKB1 is involved in HGSOC initiation and progression (4). Furthermore, it has been shown that loss-of-*Lkb1* impairs epithelial integrity and causes spontaneous cellular extrusions from epithelium (38). This process of cellular extrusion and anoikis resistance is compelling in the context of early/late cancer cell dissemination in HGSOC.

PX330 plasmids encoding sgRNAs against *Brca1, Tp53*, and *Pten* were electroporated along with a Cre expressing plasmid into the distal fallopian tube luminal epithelium of 4- to 6-week-old females; *Rosa-LSL-tdTomato* and $Lkb1^{flox/flox}$; *Rosa-LSL-tdTomato*, which will be referred to as *Lkb1* intact and *Lkb1* deletion cohorts, respectively, hereafter (**Fig. 1H**). To determine whether indel mutations were efficiently introduced into the electroporated cells, we isolated RFP^+ and RFP^- fallopian tube epithelial cells 1 month post electroporation (PE). The targeted sequences were PCR amplified and analyzed using Sanger and MiSeq sequencing. We found that only RFP^+ cells had CRISPR induced indel mutations in *Brca1, Tp53* and *Pten* while no mutations were detected in the RFP^- cells. In the isolated RFP^+ epithelial population, 100% of the sequence reads were indel mutations in *Tp53* and *Pten*, whereas only 81% were indel mutations in *Brca1* (**Fig. 1G**). Similarly, Cre-mediated deletion in *Lkb1* was only detected in the RFP^+ population but not in the RFP^- population (**Fig. 1I**). This suggested that multiple plasmids were delivered into single electroporated cells to efficiently introduce CRISPR-mediated indel mutations and Cre-mediated *Lkb1* deletion and RFP activation.

Lkb1 intact and *Lkb1* deletion cohorts both developed HGSOC with different latencies and penetrance

Following *in vivo* electroporation, we examined the distal fallopian tube and ovary of asymptomatic mice 4 months PE under a fluorescent dissecting scope. In both *Lkb1* intact and *Lkb1* deletion cohorts, RFP^+ cells were observed in the distal fallopian tube as expected (**Fig. 2A**). Interestingly, in only the *Lkb1* deletion cohort, papillary tumors developed on the ovarian surface (**Fig. 2A** and **B**). The cells in these tumors were highly proliferative as indicated by Ki67 staining (**Fig. 2C**). Within 6 months PE, widespread peritoneal metastasis formed in the *Lkb1* deletion cohort and some mice generated abdominal ascites by 7 months PE, which is a phenotype seen in approximately 30% of human patients with HGSOC (**Fig. 2D**; **Table 1**; ref. 39). Between 6 and 14 m PE, the incidence of peritoneal metastasis was 96% and the incidence of abdominal ascites was 74% in the *Lkb1* deletion cohort (**Table 1**). On the other hand, mice in the *Lkb1* intact cohort developed HGSOC at a significantly lower penetrance (21%) and later onset (**Table 1**). Ovarian tumors were observed 9 m PE and peritoneal metastasis at 11 to 16 m PE (**Table 1**). In both cohorts, peritoneal metastatic tumors were generally widespread however, larger tumors were often found in the omentum and mesentery, similar to human patients (**Fig. 2E**; refs. 40, 41). Interestingly, two patterns of peritoneal metastasis were observed; "miliary" (9/20 cases) and "oligometastatic" (11/20 cases) and recapitulated patterns seen in human patients (**Fig. 2F**; refs. 42, 43). The "miliary" pattern showed numerous millet-like lesions spreading over a wide surface of the peritoneum. This pattern is a strong negative factor with respect to overall survival in human patients. In contrast, the "oligometastatic" pattern exhibited several larger tumor nodules. These two types of metastases were not mutually exclusive and both were present in single mice similar to human patients.

Peritoneal micrometastases are undetectable by conventional imaging analysis such as MRI, PET, or CT scans and via eye inspection during surgery due to their small size. Taking advantage of our lineage tracing strategy we investigated the behavior of metastatic cells in the peritoneal environment. In a *Lkb1* deletion female 6 months PE, a relatively small ovarian tumor was formed, but there were no peritoneal metastatic nodules visible to the eye or ascites formation (**Fig. 3A**). However, under a fluorescent dissecting microscope, we detected numerous RFP^+ micrometastases in the peritoneum (**Fig. 3A**). The surface view of a relatively large RFP spot on the mesentery above the fat tissue revealed papillary tumor development on the surface of the peritoneum (**Fig. 3B**). RFP^+ cells formed a sheet-like structure with a rough surface and a papillary tumor protruded out into the peritoneal cavity. These papillary tumors were fragile and easily broken down to floating multicellular aggregates (**Fig. 3C**). We also identified small clusters of RFP^+ cells on the surface of the peritoneum, consisting of a few to a hundred RFP^+ cells (**Fig. 3D–F**). These RFP^+ clusters showed a packed morphology with a clear smooth peripheral edge in contrast to jagged cell–cell contact between mesothelial cells. The disc-like clusters often had an indentation at the center and appeared to

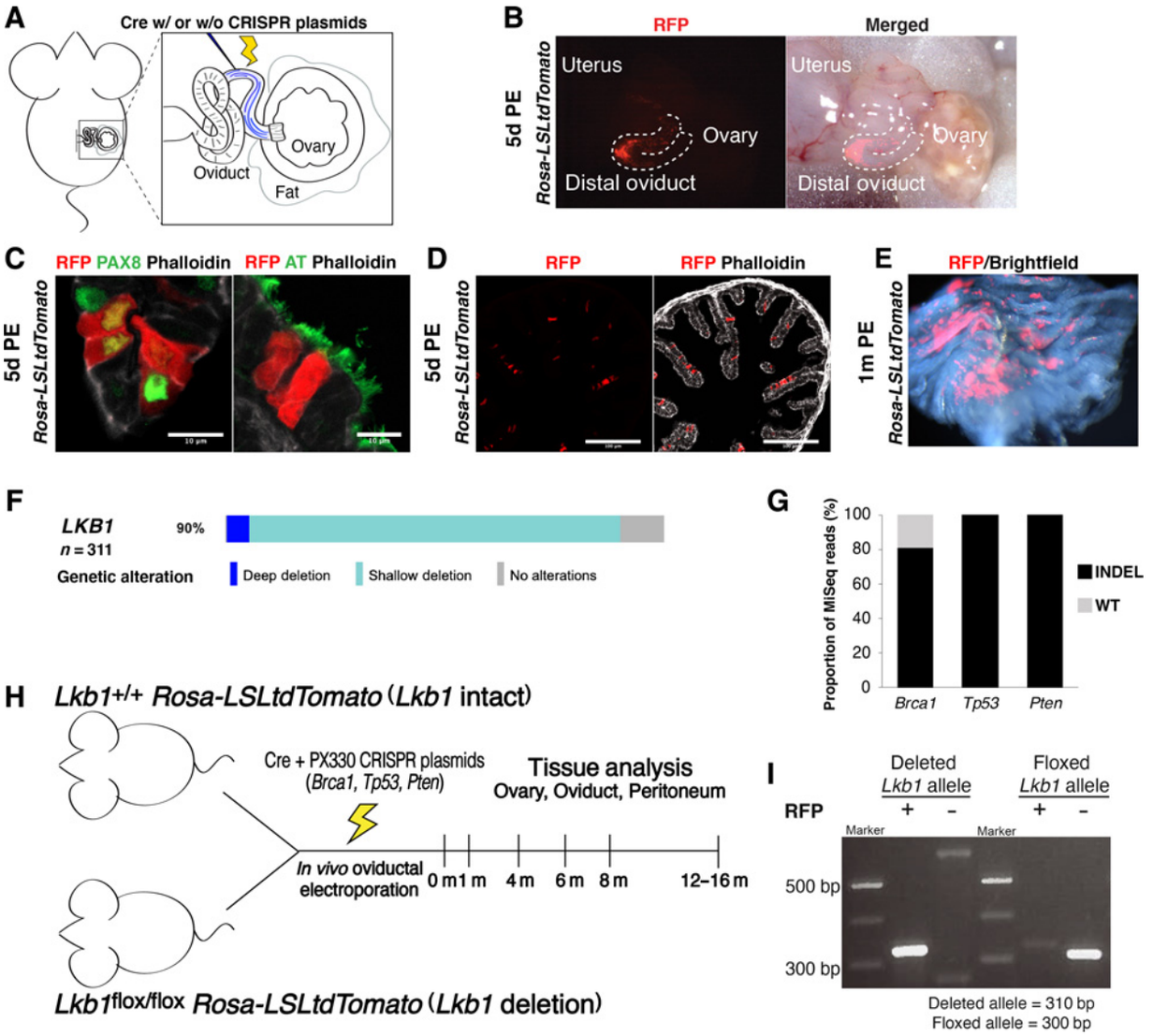

Figure 1.

In vivo fallopian tube electroporation induced Cre-mediated excision in distal fallopian tube epithelial cells of *Rosa-LSLtdTomato* mice. **A,** A diagram of the *in vivo* fallopian tube electroporation procedure. Fallopian tube/ovary was surgically exposed using a 1-cm dorsal incision. A DNA plasmid solution was injected into the fallopian tube lumen and electroporated into fallopian tube epithelial cells. **B,** RFP^+ cells within the distal fallopian tube epithelium 5 days PE in *Rosa-LSLtdTomato* mice. **C,** Transverse sections of *Rosa-LSLtdTomato* distal fallopian tube 5 days PE. Left, PAX8 (green) and phalloidin (white). Some secretory cells marked by PAX8 were RFP^+. Right, AT (green) and phalloidin (white). Some multiciliated cells marked by AT were RFP^+. Scale bar, 10 μm. **D,** Transverse section of *Rosa-LSLtdTomato* distal oviduct 5 days PE stained with phalloidin (white). RFP^+ cells were found within the luminal epithelium. Scale bars, 100 μm. **E,** Butterfly dissection of Cre-transfected regions in distal oviduct 1 m PE in *Rosa-LSLtdTomato* mouse. **F,** Oncoprint from The Cancer Genome Atlas database of *LKB1* alterations in 311 patients with ovarian serous cystadenocarcinoma. Ninety percent of these patients showed either a shallow (monoallelic loss) or deep deletion in *LKB1*. **G,** Frequency of indel mutations in MiSeq reads in RFP^+ fallopian tube epithelial cells. **H,** Schematic representation of electroporation and tissue analysis experiments in *Lkb1* intact and *Lkb1* deletion cohorts. **I,** Cre-induced *Lkb1* deletion allele was only detected in FACS sorted RFP^+ fallopian tube epithelial cells but not in RFP^- cells 1 m PE.

penetrate the basal membrane underneath the mesothelium (**Fig. 3D**, **E**, and **G**). Recruitment and activation of innate immune cells (e.g., $LYVE1^+$ tissue residential macrophages) was observed immediately underneath the clusters (**Fig. 3E**). Stress fiber-like F-actin structures at the bottom of the RFP^+ cells would suggest activation of integrins and ECM remodeling (**Fig. 3F**).

Immunohistochemical analysis and pathologic review were performed on ovarian and peritoneal tumors in both cohorts. In the *Lkb1* intact cohort, these tumors were papillary and expressed PAX8, WT1, and CK8 (**Fig. 4A**), similar to HGSOC profiles in human patients (44) and consistent with the previously reported animal models (7, 45). In the *Lkb1* deletion cohort, most tumors also showed papillary architecture and approximately 15% of these tumors expressed PAX8, WT1, and CK8 (**Fig. 4B**); however, a significant portion (80%) of them were $PAX8^-$, $WT1^+$, and $CK8^+$ (**Fig. 4C**). It was also noted that 26% of these mice developed a rare form of ovarian cancer called ovarian carcinosarcomas or malignant mixed Müllerian tumors (MMMT; **Fig. 4D**), which was also reported in the *Ovgp1-iCreER*^{T2} model by

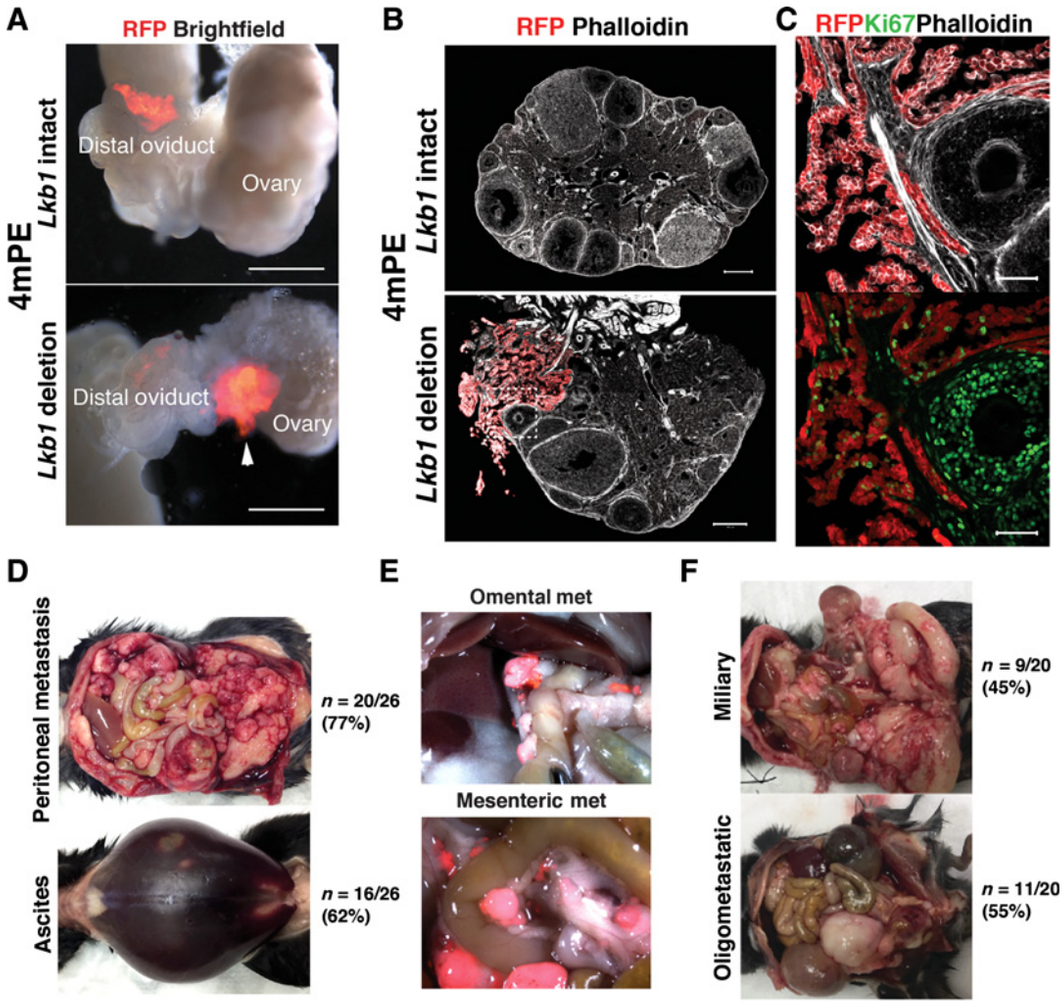

Figure 2.

Formation of papillary ovarian tumors, peritoneal metastasis, and ascites in *Lkb1* deletion cohort. **A,** Dissection scope images of ovary and fallopian tube of *Lkb1* intact and *Lkb1* deletion mice 4 m PE. RFP$^+$ ovarian tumor (white arrowhead) was only detected on the ovary of an *Lkb1* deletion female. Scale bars, 500 μm. **B,** Sections of ovaries from *Lkb1* intact and *Lkb1* deletion mice 4 m PE stained with phalloidin (white). Papillary tumor (red) on the ovary of a *Lkb1* deletion female. Scale bars, 200 μm. **C,** Higher magnification image of inset marked in **B**. Many cells in the papillary tumor (red) were Ki67$^+$ (green). Scale bars, 50 μm. **D,** Peritoneal metastasis and abdominal ascites formation. **E,** RFP$^+$ metastatic omental and mesenteric tumors. **F,** Two types of peritoneal metastasis (miliary and oligometastatic) in *Lkb1* deletion mice.

Zhai and colleagues (45). Here, we have shown that HGSOC tumorigenesis can be induced by targeting *Brca1, Tp53*, and *Pten* in the oviductal epithelial cells using *in vivo* electroporation. Interestingly, loss-of-*Lkb1* along with mutations in *Brca1, Tp53*, and *Pten* facilitated HGSOC initiation and progression and these mice often presented with abdominal ascites; however, many of these tumors were PAX8$^-$.

Frameshift mutations of the targeted tumor suppressor genes were predominantly selected in ovarian tumors and peritoneal metastases

CRISPR-induced indel mutations are relatively random (25, 46, 47); therefore, the genotype of individual electroporated cells soon after electroporation can, theoretically, vary in our models. If a combination of mutations in a cell gains a proliferative and/or survival advantage, the cell can form a clone in the epithelium and with further genetic and epigenetic alterations, some clones will progress to form ovarian tumors and peritoneal metastasis (Supplementary Fig. S2A).

Analyses of mutation types in our targeted genes were performed using MiSeq amplicon sequencing of the targeted loci (*Brca1, Tp53, Pten* exon 5, and *Pten* exon 7) in ovarian tumors and 1 to 3 metastatic lesions from individual mice in *Lkb1* intact and *Lkb1* deletion cohorts (Supplementary Fig. S2B). From the samples analyzed, the majority of the mutations detected in *Brca1, Tp53*, and *Pten* were frameshift mutations in both *Lkb1* intact and *Lkb1* deletion mice (Supplementary Fig. S2C). Wild-type reads were also detected, suggesting contamination of normal surrounding cells like stromal and hematopoietic cells, as well as nonmutated alleles in tumor cells. Interestingly, in one *Lkb1* intact mouse (4450822), no *Brca1* mutations were detected in the ovarian tumor and peritoneal metastasis, suggesting that *Brca1* mutations were not absolutely required for tumorigenesis in our model and that a combination of *Tp53* and *Pten* mutations were sufficient to induce HGSOC (Supplementary Fig. S2C). On the other hand, some peritoneal metastases in one *Lkb1* deletion mouse (40912) had no mutations in *Brca1* and *Tp53*, suggesting that a combination of loss-of-

Table 1 . Summary of disease progression in *Lkb1* intact and *Lkb1* deletion cohorts.

Month(s) post electroporation	Ovarian tumor incidence (per ovary)	Peritoneal metastasis (per mouse)	Ascites formation (per mouse)
Lkb1 intact			
1	0/2 (0%)	0/1 (0%)	0/1 (0%)
4–5	0/8 (0%)	0/4 (0%)	0/4 (0%)
6–8	0/16 (0%)	0/8 (0%)	1/8 (12.5%)
9–10	1/8 (12.5%)	0/4 (0%)	0/4 (0%)
11–14	5/18 (27.8%)	2/9 (22.2%)	2/9 (22.2%)
15–16	1/8 (12.5%)	1/4 (25%)	0/4 (0%)
Lkb1 deletion			
1	0/2 (0%)	0/1 (0%)	0/1 (0%)
4–5	5/8 (62.5%)	0/4 (0%)	0/4 (0%)
6–8	13/16 (81.3%)	7/8 (87.5%)	4/8 (50%)
9–10	17/18 (94.4%)	9/9 (100%)	8/9 (88.9%)
11–14	12/12 (100%)	6/6 (100%)	5/6 (83.3%)

Lkb1 and *Pten* mutations would be sufficient to induce HGSOC progression in the *Lkb1* deletion cohort (Supplementary Fig. S2C).

PAX8$^-$ papillary tumors developed in the *Lkb1* deletion cohort originated from the OSE and hilum region

Although the *Lkb1* deletion cohort developed HGSOC with peritoneal metastasis at a shorter latency and higher penetrance, many tumors in these mice were PAX8$^-$ (**Fig. 4C**). Recently, Zhang and colleagues and Lõhmussaar and colleagues have suggested that both the FTE and OSE in mice have the potential to develop HGSOC (5, 6). Interestingly in the model developed by Zhang and colleagues, the tumors developed from the FTE were PAX8$^+$ while the tumors derived from the OSE were PAX8$^-$. Therefore, we hypothesized that the PAX8$^-$ tumors developed in the *Lkb1* deletion cohort likely originated from the small population of targeted OSE/ovarian hilum cells (Supplementary Fig. S1).

To determine the origin of the tumors formed in the *Lkb1* deletion cohort, we performed salpingectomies (fallopian tube removal) and ovariectomies (ovary removal) immediately after electroporation in 4- to 6-week-old *Lkb1*$^{flox/flox}$; *Rosa-LSLtdTomato* females. Interestingly, the salpingectomized mice still developed large ovarian tumors with widespread peritoneal metastasis at a similar latency to non-salpingectomized mice at 6 to 7 m PE (Supplementary Table S1). Papillary tumors were found in the OSE and hilum regions 6 m PE (**Fig. 5A**). These tumors, along with the ovarian and peritoneal tumors that formed, were PAX8$^-$, WT1$^+$, and CK8$^+$ (**Fig. 5A**).

On the other hand, in the ovariectomized mice, RFP$^+$ growths in the FTs were observed (**Fig. 5B**); however, peritoneal metastasis did not form 6 to 10 m PE (Supplementary Table S1). It is unknown if the ovary is required for metastatic tumor formation or whether 10 months was not long enough to allow development of peritoneal metastasis from the FTE. Interestingly, STIC-like precancerous lesions were observed in the distal FTE of ovariectomized mice (**Fig. 5C**).

On the basis of these observations, we examined the expression of GATA4, a marker for the OSE, in the tumors developed in the *Lkb1* deletion cohort (Supplementary Fig. S2). Consistent with the results above, most of the PAX8$^-$ tumors were GATA4$^+$ (**Fig. 5D**, Supplementary Fig. S2), suggesting their OSE origin. Most notably, MMMTs were GATA4$^-$ while the epithelial structure of the tumors was PAX8$^+$, suggesting an FTE origin (**Fig. 5E**).

Formation of fallopian tube precancerous lesions in both *Lkb1* intact and deletion cohorts with rapid development of papillary tumors in the OSE of *Lkb1* deletion mice

Interestingly, despite the fact that we performed the same electroporation procedure targeting the distal fallopian tube in both *Lkb1* intact and deletion cohorts, the tumors that developed were from different cell populations; FTE and OSE, respectively. This suggested that the FTE and OSE have distinct susceptibility to the two different mutation combinations. To evaluate this, we examined the early cellular responses in the FTE and OSE against each mutation combination.

By 4 m PE, secretory cell out growths (SCOUT)-like lesions were detected in the fallopian tube in both *Lkb1* intact and *Lkb1* deletion cohorts, marked by PAX8, WT1, and CK8 (**Fig. 6A**). RFP$^+$ SCOUTs retained in the epithelium displayed epithelial disorganization compared with normal FTE (**Fig. 6A–C**) and increased cross-sectional area per cell compared with adjacent RFP$^-$ and RFP$^+$ non-SCOUT cells (**Fig. 6C** and **D**). This phenotype was further exacerbated with loss-of-*Lkb1* since cross sectional area per cell in RFP$^+$ SCOUT forming cells in *Lkb1* deletion mice were larger than *Lkb1* intact RFP$^+$ SCOUT cells (**Fig. 6D**). These lesions expressed PAX8 and an enrichment of membrane pAKT (**Fig. 6A** and **E**), suggesting the activation of AKT as a consequence of PTEN loss-of-function. Although they showed coherent colonies, suggesting an expansion of the RFP$^+$ cells, we did not find an enrichment of Ki67 staining in these early lesions; however, STICs in later stages were highly proliferative (**Fig. 6F**). The morphology of these coherent PAX8 colonies were quite similar to reported human SCOUTs (48, 49).

To examine the early cellular responses in the OSE, we intentionally targeted the OSE because the number of electroporated cells within the OSE was too small using our standard FTE targeting procedure. In as early as 2 months PE, papillary tumor formation from the OSE was observed in the *Lkb1* deletion cohort while no clonal growth of RFP$^+$ cells was observed in the *Lkb1* intact cohort (**Fig. 6G**). Consistent with a previous study (50), we found that a combination of loss-of-*Lkb1* and *Pten* alone was sufficient for papillary tumor formation in the OSE (**Fig. 6G**). Similar to the fallopian tube lesions, RFP$^+$ papillary tumor cells showed an enrichment of membrane pAKT (**Fig. 6H**).

These data suggested that the electroporated cells in either the OSE or FTE activated the AKT/mTOR pathway; however, only the cells in the OSE rapidly developed papillary tumors with a high frequency while the cells in the FTE showed only precancerous changes that would need more time for additional oncogenic alterations and progression to develop into HGSOC.

Multiomic analysis reveals similarities to human tumor copy number profiles and ascitic fluid cellular constituents

To investigate the similarities of our tumors to human HGSOC, we undertook whole genome sequencing of a selection of tumors from *Lkb1* intact/deletion cohorts and varying PAX8 statuses. Focusing on CNAs (copy number alterations), which are the recurrent defining genomic feature of HGSOC, we identified amplifications and deletions in all samples (**Fig. 7A**; Supplementary Table S2). Half of the tumors examined had significantly more CNAs, which corelated with PAX8 expression but not significantly with *Lkb1* status, tumor cell purity or age (**Fig. 7A–C**). These tumors likely originated from the FTE and indicates that the cell-of-origin can influence genomic changes in our model. In addition, we found that common CNAs identified in human HGSOC were also found in our tumors (**Fig. 7D**).

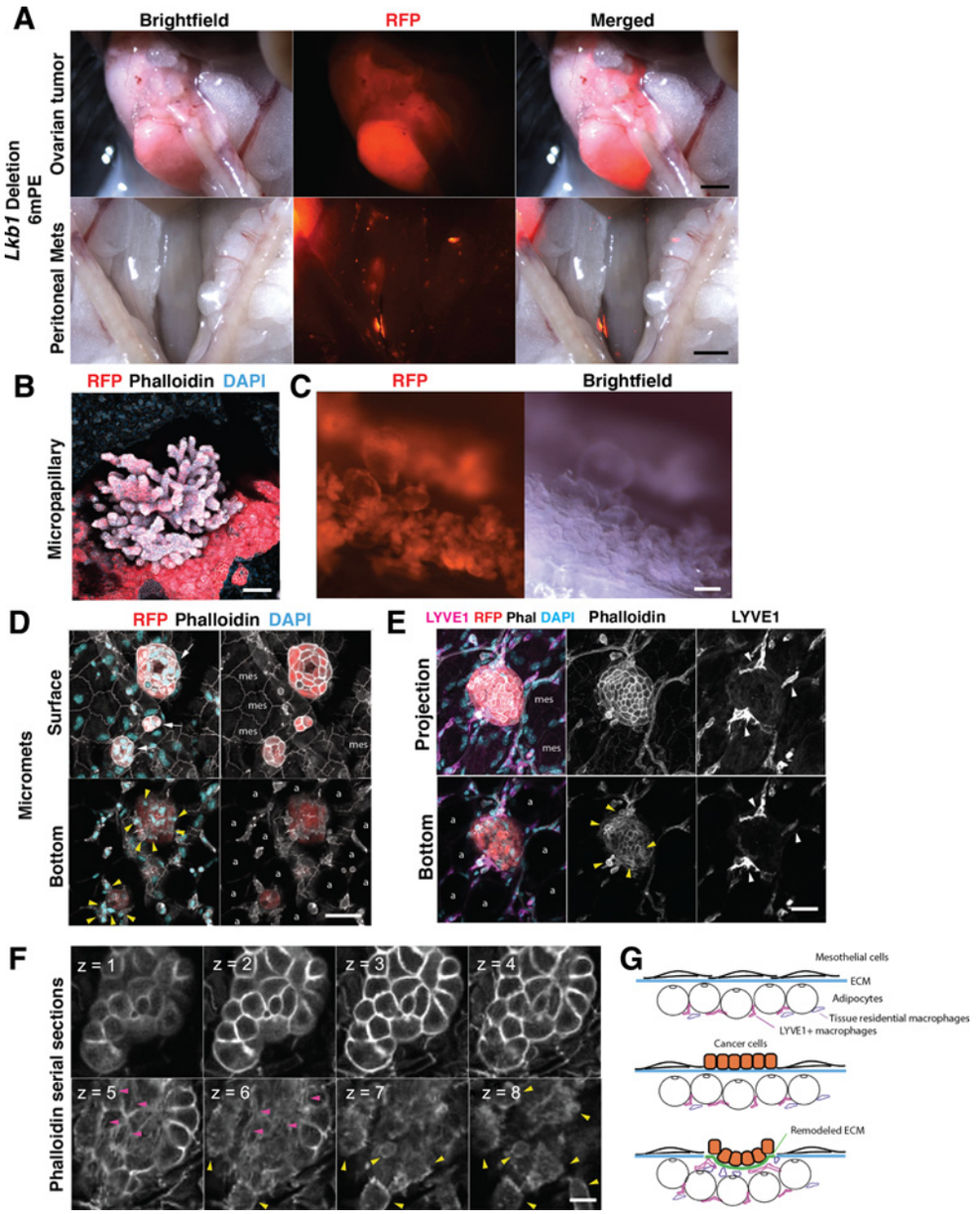

Figure 3.

Visualization of peritoneal micrometastases. **A,** Dissection scope images of primary ovarian tumor and peritoneal micrometastases in a *Lkb1* deletion female 6 m PE. Scale bars, 5 μm. No visible metastatic nodule in the brightfield image, while numerous micrometastases were detected in the RFP image of the peritoneum. **B,** A confocal projected image of a micropapillary metastasis on the peritoneum. Scale bar, 100 μm. **C,** Papillary micrometastases spread on the peritoneum. These tumors were fragile and easily broken down to floating multicellular aggregates. Scale bar, 100 μm. **D,** Three micrometastases on the peritoneum. Surface and bottom section images. Surface mesothelial cells (mes) show characteristic jagged cell–cell contact and flat cell morphology. The micrometastases (white arrows) formed a packed disc-like morphology with a central indentation. Underneath the metastases, macrophage-like cells were observed (yellow arrowheads). a, adipocytes. Scale bar, 50 μm. **E,** LYVE1^{+} (pink) tissue residential macrophages near micrometastases (white arrowheads). Protrusive structures from LYVE1^{+} cells spread under the disc-like micrometastasis. Scale bar, 50 μm. **F,** Phalloidin serial confocal section images. 1.5 μm section intervals. Stress fiber–like F-actin structure at the bottom of the micrometastasis (Z = 5,6; magenta arrowheads). Scale bar, 10 μm. **G,** A diagram of peritoneal metastasis formation. Top, healthy peritoneum. Thin mesothelial cells on the ECM membrane (blue) lining the visceral peritoneum in omentum and mesentery. Middle, mesothelial clearance. Cancer cells integrate into the mesothelial layer. Bottom, tissue residential macrophages (LYVE1^{+}) are recruited. The cancer cells and the recruited macrophages remodel the ECM underneath the cancer cells (green).

The build-up of ascitic fluid is a common presentation in patients with HGSOC and is thought to facilitate tumor cell dissemination throughout the peritoneal cavity (51). It is unknown however if mouse models faithfully recapitulate the ascites environment. To investigate the cellular make up of ascites in mice, we conducted single cell RNA sequencing of ascites isolated from a single mouse in our *Lkb1* deletion

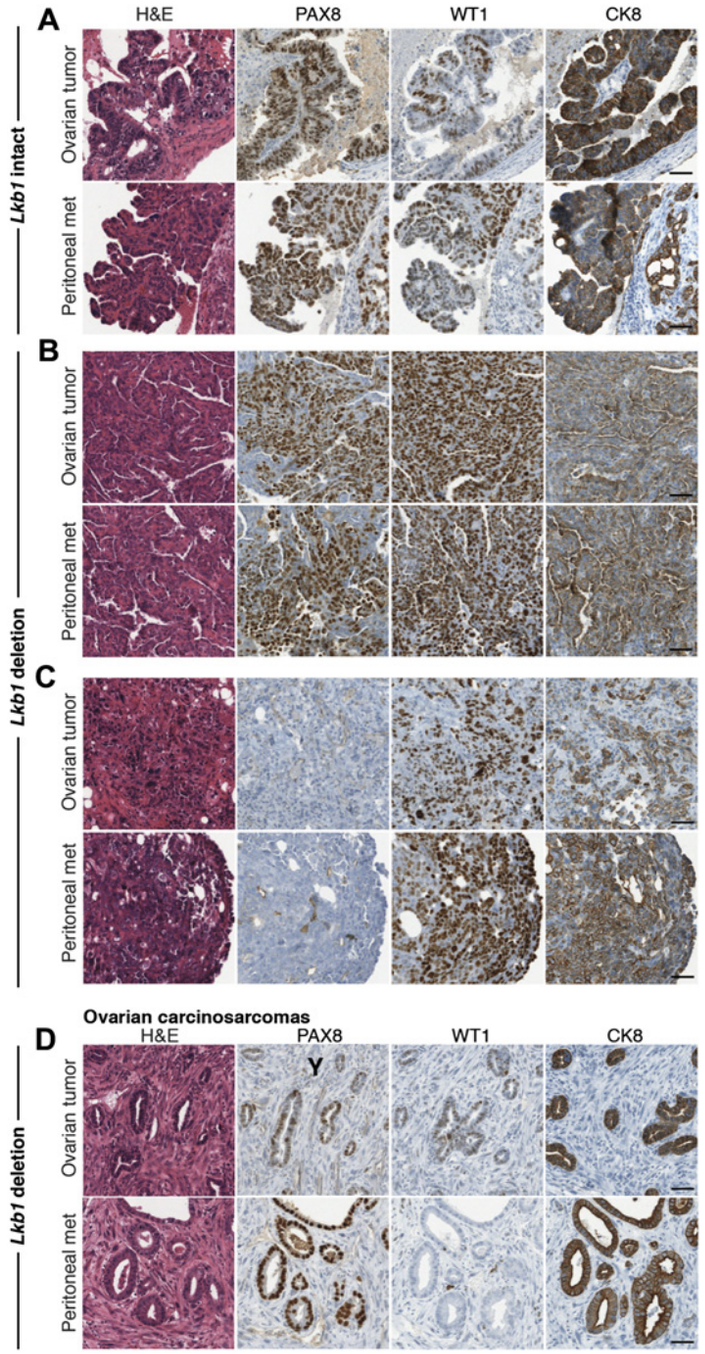

Figure 4.

Histology of HGSOC tumors and metastatic peritoneal tumors in *Lkb1* intact and *Lkb1* deletion cohorts. H&E, PAX8, WT1, and CK8 immunohistochemical staining in ovarian and peritoneal tumors. **A,** *Lkb1* intact mice. Ovarian and peritoneal tumors expressed PAX8, WT1, and CK8. **B,** *Lkb1* deletion mice. **C,** Ovarian and peritoneal tumors expressed PAX8, WT1, and CK8 *Lkb1* deletion mice. Ovarian and peritoneal tumors expressed WT1 and CK8 but not PAX8. **D,** Ovarian carcinosarcomas in *Lkb1* deletion mice. Scale bars, 50 μm.

cohort (#50822). Single cells (4,556) were identified and clustered into 9 populations with distinct transcriptomic profiles (**Fig. 7E**). On the basis of the expression of specific markers, we identified populations of macrophages (*Csf1r*$^+$), monocytes (*Cd14*$^+$), tumor cells (*Epcam*$^+$ and *Tdtomato*$^+$), B cells (*Cd79a*$^+$), dividing cells (*Ccna2*$^+$), T cells (*Cd3d/e/g*$^+$), erythrocytes (*Gypa*$^+$), and cancer-associated fibroblasts (*Col1a1*$^+$; **Fig. 7E–G**; Supplementary Table S3). The tumor cells displayed significant CNAs consistent with their malignant state compared with few CNAs identified in host cells and had high expression of OSE markers (*Gata4, Gata6*, and *Unc45b*) but low expression of FTE markers (*Pax8, Ltf*, and *Slc34a2*; **Fig. 7H–J**; Supplementary Tables S3 and S4). It has been previously shown that expression of FTE and OSE markers is retained in tumors originating from these sites, suggesting an OSE origin of this tumor (5). The cellular make up of human HGSOC ascites has been found to contain predominantly immune cells with macrophages/monocytes being the dominant cell type and few tumor cells or cancer-associated fibroblasts (52, 53). From our single-cell analysis, we also identified an environment dominated by macrophages/monocytes with similar proportions to human HGSOC ascites (**Fig. 7G**). Although we have

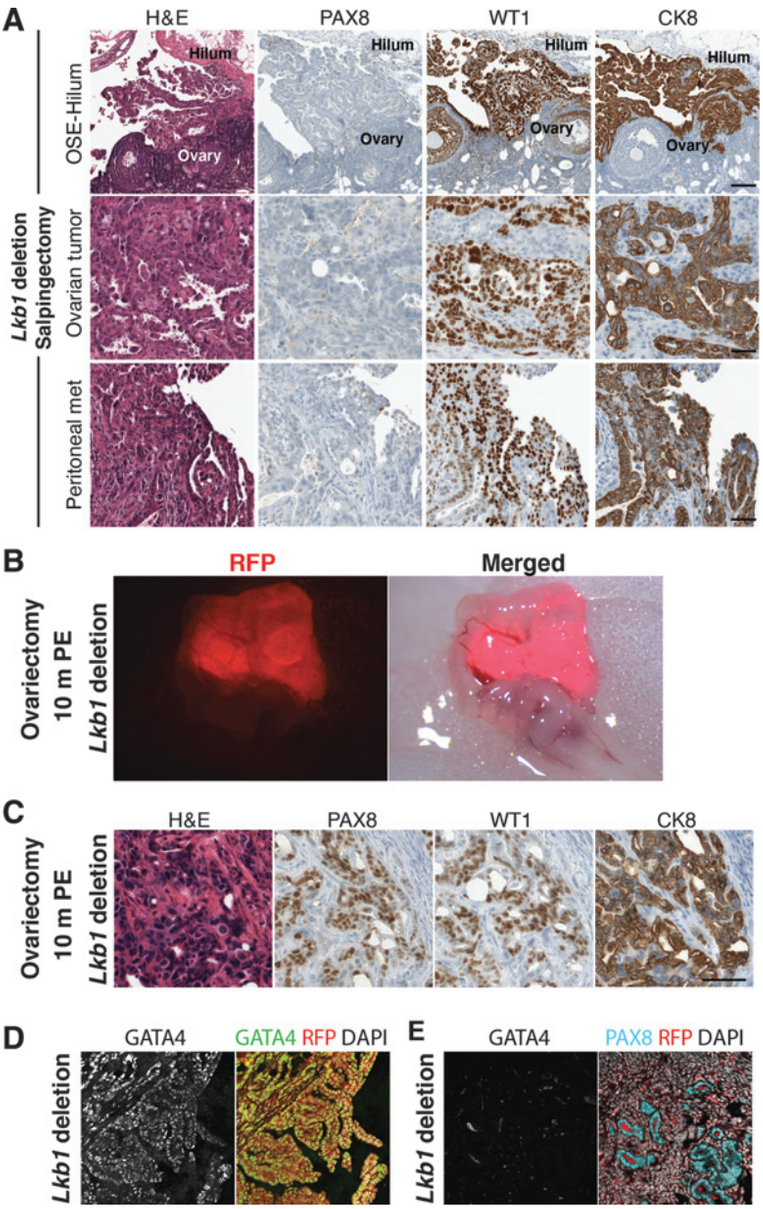

Figure 5.

HGSOC tumors developed in *Lkb1* deletion mice originated from the OSE and hilum region. **A,** H&E, PAX8, WT1, and CK8 immunohistochemical staining in tumors formed in salpingectomized *Lkb1* deletion mice (top). Papillary tumor formation from the OSE-hilum region. These tumors were PAX8$^-$, WT1$^+$, and CK8$^+$. Scale bars, 100 μm. Middle and bottom, ovarian and peritoneal tumors were also PAX8$^-$, WT1$^+$, and CK8$^+$. Scale bars, 50 μm. **B,** RFP$^+$ growth within the distal FT of ovariectomized *Lkb1* deletion mouse 10 m PE. **C,** H&E, PAX8, WT1, and CK8 immunohistochemical staining of STIC formed in the fallopian tube in ovariectomized *Lkb1* deletion mouse. These STICs were PAX8$^+$, WT1$^+$, and CK8$^+$. **D,** *Lkb1* deletion tumors stained for GATA4 and DAPI. **E,** Papillary tumors were GATA4$^+$ (left, white; right, green) MMMTs stained for GATA4, PAX8, and DAPI. These tumors were GATA4$^-$, while the epithelial structure of the tumors were PAX8$^+$ (blue).

only analyzed an ascites sample from a single mouse, there is a possibility of variation between mice, as seen between patients; however, the similarities in ascitic fluid cellular constituents compared with human samples suggests GEMMs of HGSOC have the potential to be a good model for this stage of HGSOC progression.

Discussion

In this study, we developed a unique strategy to generate mouse ovarian cancer models that recapitulate human disease by using *in vivo* fallopian tube electroporation, CRISPR/Cas9-mediated genome editing, and Cre-mediated lineage tracing. Using *in vivo* electroporation, the target area was limited to the distal fallopian tube and ovary, leaving the rest of the female reproductive tract and other tissues/organs unmodified. In contrast to the *Pax8-TetOn-Cre* and *Ovgp1-iCreERT2* mouse models, there was no risk of developing tumors in nontargeted tissues/organs, which may necessitate early euthanasia prior to observing symptoms related to HGSOC (5, 7, 45). The targeting area in this method can also be easily changed by using different sized tweezer type electrodes. The density of electroporated cells can also be modified by changing electroporation parameters and plasmid concentrations. In contrast to systemic Cre activation, which uniformly impacts all Cre-expressing cells in targeted tissues, electroporation can create a random mosaic pattern of normal and mutated cells within an epithelium (**Fig. 1D**). This mosaic pattern more closely resembles human carcinogenesis, which likely occurs in a local sporadic manner. In addition, various regions of the female reproductive system can be easily targeted with different mutation combinations. This high level of flexibility in choosing gene targets and areas will be useful in developing somatic GEMMs for HGSOC (19, 21), which is genetically highly heterogeneous, as well as other types of OCs in which the cell-of-origin and causative mutations are not fully defined (54, 55).

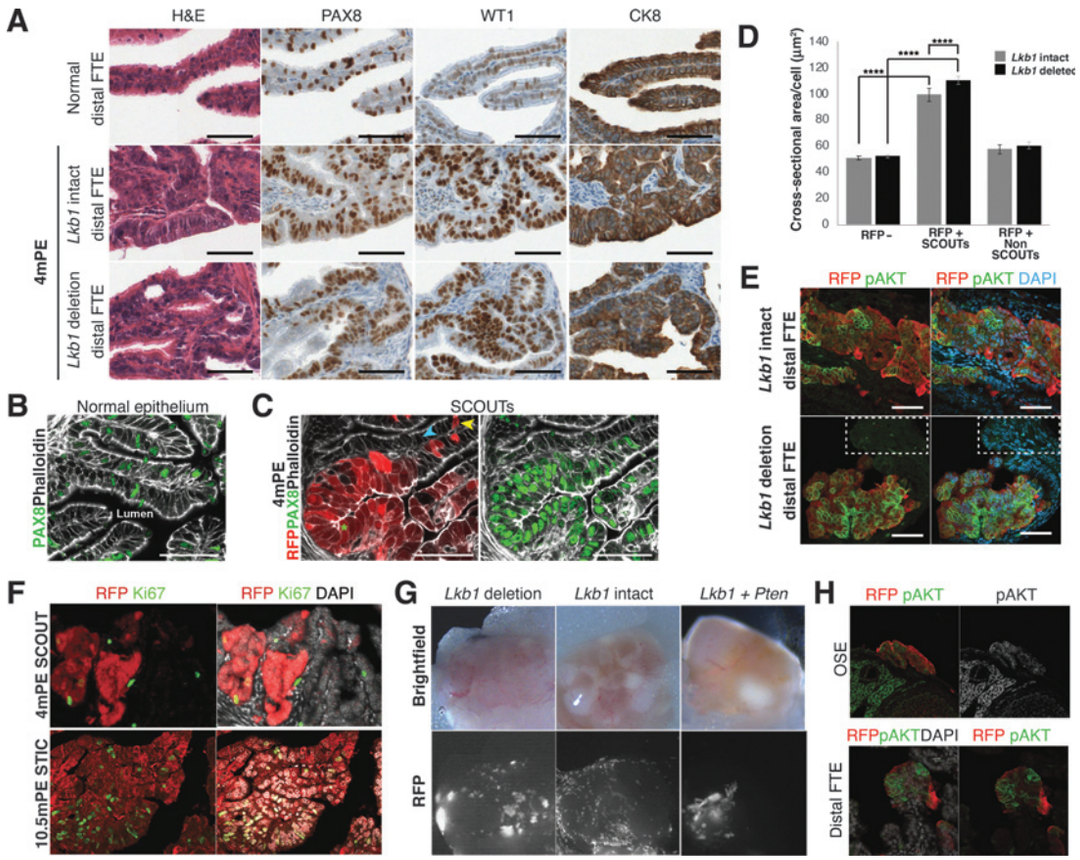

Figure 6.

Lkb1 intact and *Lkb1* deletion FTs developed SCOUT-like lesions 4 m PE. **A,** H&E, PAX8, WT1, and CK8 immunohistochemical staining of normal distal fallopian tube. SCOUT-like lesions in both *Lkb1* intact and *Lkb1* deletion FTs 4 m PE. Scale bars, 50 µm. **B,** Normal fallopian tube epithelium stained with phalloidin (white) and PAX8 (green). PAX8 secretory cells are randomly distributed throughout the epithelium. Scale bars, 50 µm. **C,** RFP^+ SCOUT-like lesion within the fallopian tube epithelium stained with phalloidin (white) and PAX8 (green) in *Lkb1* deletion mouse 4 m PE. The SCOUT-like lesions displayed epithelial disorganization and expressed PAX8 (green). Blue arrowhead, RFP^- cell; green asterisk, SCOUT forming RFP^+ cell; yellow arrowhead, RFP^+ non-SCOUT cell. Scale bars, 50 µm. The images in **B** and **C** were cropped from the same large image. **D,** A bar graph of the cross-sectional area per cell of RFP^- cells, RFP^+ cells within SCOUTs and RFP^+ cells outside SCOUTs in *Lkb1* intact and *Lkb1* deleted FT STICs. **E,** SCOUT-like lesions in distal FTE of *Lkb1* intact and *Lkb1* deletion mice stained for pAKT (green) and DAPI (blue). RFP^+ cells express membrane pAKT. Dotted box outlines RFP^- cells that do not express pAKT. Scale bars, 50 µm. **F,** SCOUT-like lesions (red) 4 m PE did not show frequent $Ki67^+$ cells compared with STIC-like lesions 10.5 m PE. RFP (red), Ki67 (green), DAPI (white). **G,** RFP^+ colonies growing on the OSE 2 m PE in the *Lkb1* deletion and *Lkb1* + *Pten* deleted females but not in the *Lkb1* intact females. **H,** Early papillary tumors on the OSE 2 m PE in a *Lkb1* deleted female stained for pAKT.

On the other hand, this strategy has some limitations. First, using the current method, it is not possible to target specific cell lineages. This can be overcome by controlling Cas9 and Cre expression using a specific cell promoter such as *Ovgp1* or *Pax8*. Second, this strategy initially generates heterogeneous mutation patterns of selected genes in the target cell population. This means that each mouse is a unique cancer model, similar to human patients. For this reason, this method would be difficult to use directly as preclinical models for systematic evaluation of specific therapeutics. However, this initial mutational variation could potentially provide very important information on tumor evolution and emergence of tumor subtypes as previously reported in the pancreatic cancer modeling using CRISPR-mediated genome editing (56). To take advantage of CRISPR-mediated cancer modeling, cell lines should be established. These lines have higher diversity in mutation patterns but are still less complex than human samples, which would be useful for systemic evaluation of therapeutics.

The presented approach also easily incorporates the Cre reporter system into mouse cancer models to track genetically modified cells. In other HGSOC mouse models (3, 7, 45, 50), peritoneal metastatic tumors are detected when the tumor has grown to a size that can be visible. We identified microscopic metastases in the peritoneum via detection of Cre-mediated RFP expression in cancer cells. Various useful Cre reporter lines are available, such as Confetti (57, 58) and Fucci (59, 60), to track clonal patterns of Cre-activated cells and to visualize cell cycles, respectively. These mice will be highly useful to study clonal evolution and mechanisms of peritoneal metastasis formation. Although immunogenicity of transgenes would be a concern from using transgene-based lineage tracing in cancer models, this would be conquered by expressing nonfunctional transgenes to induce immune tolerance (61).

The peritoneum is the primary metastatic site for HGSOC. Most patients with HGSOC are diagnosed at advanced stages when tumors

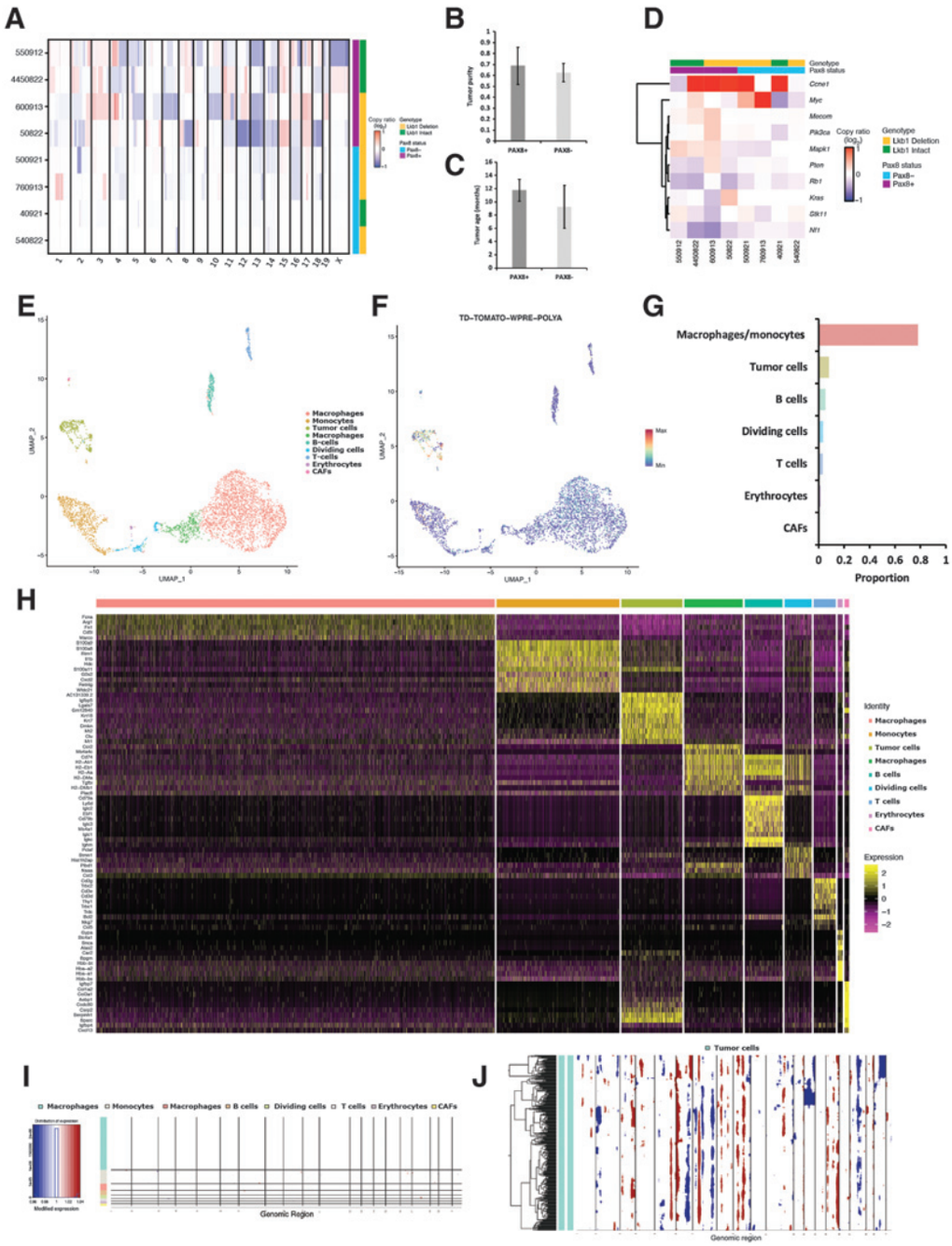

Figure 7.

HGSOC tumors recapitulate copy number changes and ascites environment. **A,** The copy number changes identified in 8 tumors of varying *Lkb1* and PAX8 statuses using whole genome sequencing and 20 kb bin sizes; see Supplementary Table S2 for a complete list of regions affected. **B,** A comparison of tumor cell purity between sequenced PAX8$^+$ and PAX8$^-$ tumors. **C,** A comparison of tumor age between sequenced PAX8$^+$ and PAX8$^-$ tumors. **D,** The copy number profiles of a section of genes previously identified to undergo copy number alterations in human HGSOC tumors. **E,** The cellular composition of ascites was investigated using scRNA sequencing. Individual cells (4,556) were identified and clustered into 9 distinct clusters. **F,** Tumor cells were identifiable by the expression of transcripts aligning to the *Tdtomato-WPRE-polyA* stranscript. **G,** Quantification of the different cell types in the ascites identified an environment dominated by macrophages. **H,** A heatmap showing the most differentially expressed genes within each cluster. See Supplementary Table S3 for a complete list. **I,** A copy number analysis performed using the inferCNV package identified few CNVs in host cells. **J,** Significant CNVs were identified in tumor cells; see Supplementary Table S4 for a complete gene list. No significant difference was detected in **B** and **C** using two-tailed Student *t* test ($P > 0.05$).

cells have already spread to the peritoneal cavity (62–65). However, our knowledge of how cancer cells interact with the peritoneum is still limited. The peritoneal micrometastases we observed in our models suggests the potential involvement of tissue-residential macrophage/dendritic cells in this process. Further studies will be essential to understand the cellular and molecular mechanisms of peritoneal metastasis formation in HGSOC.

Two types of peritoneal metastatic patterns are known; oligometastatic and miliary. It is also known that there is an association between dissemination pattern in the peritoneal cavity and median overall survival in which patients with an upper abdominal/miliary dissemination phenotype have a shorter median overall survival (66, 67). The exact cause for different dissemination patterns in HGSOC is unknown but could be driven by a combination of different genomic aberrations and host–tumor interactions. The use of mouse models that can generate miliary metastatic patterns of ovarian cancer, such as the model we present here, will be highly useful to investigate the complex biology of peritoneal metastasis of HGSOC *in vivo*.

Taken together, our results indicate that different cell types have distinct susceptibilities based on the combination of genetic alterations introduced. Understanding how the cell-of-origin of HGSOC contributes to phenotypic heterogeneity, pathophysiology and subsequently, histotype, will be critical in determining correct diagnostic classification and development of effective strategies for prevention, prognosis, and treatment of HGSOC.

Authors' Disclosures

No disclosures were reported.

Authors' Contributions

K. Teng: Data curation, investigation, methodology, writing–original draft, writing–review and editing. **M.J. Ford:** Data curation, investigation, writing–review and editing. **K. Harwalkar:** Data curation, investigation. **Y. Li:** Data curation, investigation. **A.S. Pacis:** Data curation. **D. Farnell:** Validation, pathological review. **N. Yamanaka:** Methodology. **Y.-C. Wang:** Data curation, single cell analysis. **D. Badescu:** Data curation, single cell analysis. **T.N. Ton Nu:** Data curation, validation, pathological review. **J. Ragoussis:** Conceptualization, supervision, funding acquisition, writing–review and editing. **D.G. Huntsman:** Supervision, validation, pathological review. **J. Arseneau:** Data curation, validation, pathological review. **Y. Yamanaka:** Conceptualization, data curation, supervision, funding acquisition, writing–review and editing.

Acknowledgments

The authors thank the McGill Goodman Cancer Research Centre Histology and Flow Cytometry Cores. They also thank the McGill Advanced Bioimaging Facility (ABIF). This work was supported by Canadian Cancer Society (CCS) Innovation grant (Haladner Memorial Foundation #704793), CCS i2I grant (#706320), and Cancer Research Society Operation Grant (#23237). K. Teng was supported by MICRTP and Canderel studentships. M.J. Ford was supported by Canderel, CRRD, and FRQS postdoc fellowships. K. Harwalkar was supported by CRRD and Alexander McFee (Faculty of Medicine) and Gosselin studentships. Y. Li was supported by Canderel studentship.

Received May 10, 2020; revised September 16, 2020; accepted July 21, 2021; published first July 23, 2021.

References

1. American Cancer Society. Cancer facts & figures 2021. Atlanta, GA: American Cancer Society; 2021.
2. Bowtell DD, Bohm S, Ahmed AA, Aspuria P-J, Bast RC Jr, Beral V, et al. Rethinking ovarian cancer II: reducing mortality from high-grade serous ovarian cancer, Nat Rev Cancer 2015;15:668–79.
3. Kim J, Coffey DM, Creighton CJ, Yu Z, Hawkins SM, Matzuk MM. High-grade serous ovarian cancer arises from fallopian tube in a mouse model. Proc Natl Acad Sci U S A 2012;109:3921–6.
4. George SHL, Milea A, Sowamber R, Chehade R, Tone A, Shaw PA. Loss of LKB1 and p53 synergizes to alter fallopian tube epithelial phenotype and high-grade serous tumorigenesis. Oncogene 2016;35:59–68.
5. Zhang S, Dolgalev I, Zhang T, Ran H, Levine DA, Neel BG. Both fallopian tube and ovarian surface epithelium are cells-of-origin for high-grade serous ovarian carcinoma. Nat Commun 2019;10:5367.
6. Lõhmussaar K, Kopper O, Korving J, Begthel H, Vreul CPH, van Es JH, et al. Assessing the origin of high-grade serous ovarian cancer using CRISPR-modification of mouse organoids. Nat Commun 2020;11:2660.
7. Perets R, Wyant GA, Muto KW, Bijron JG, Poole BB, Chin KT, et al. Transformation of the Fallopian tube secretory epithelium leads to high-grade serous ovarian cancer in Brca;Tp53;Pten models. Cancer Cell 2013;24:751–65.
8. Kroeger PT Jr, Drapkin R. Pathogenesis and heterogeneity of ovarian cancer. Curr Opin Obstet Gynecol 2017;29:26–34.
9. Kauff ND, Barakat RR. Risk-reducing salpingo-oophorectomy in patients with germline mutations in BRCA1 or BRCA2. J Clin Oncol 2007;25:2921–7.
10. Greene MH, Piedmonte M, Alberts D, Gail M, Hensley M, Miner Z, et al. A prospective study of risk-reducing salpingo-oophorectomy and longitudinal CA-125 screening among women at increased genetic risk of ovarian cancer: design and baseline characteristics: A Gynecologic Oncology Group study. Cancer Epidemiol Biomarkers Prev 2008;17:594–604.
11. Lee Y, Miron A, Drapkin R, Nucci MR, Medeiros F, Saleemuddin A, et al. A candidate precursor to serous carcinoma that originates in the distal fallopian tube. J Pathol 2007;211:26–35.
12. Shaw PA, Rouzbahman M, Pizer ES, Pintilie M, Begley H. Candidate serous cancer precursors in fallopian tube epithelium of BRCA1/2 mutation carriers. Mol Pathol 2009;22:1133–8.
13. Medeiros F, Muto MG, Lee Y, Elvin JA, Callahan MJ, Feltmate C, et al. The tubal fimbria is a preferred site for early adenocarcinoma in women with familial ovarian cancer syndrome. Am J Surg Pahtol 2006;30:230–6.
14. Soong TR, Howitt BE, Miron A, Horowitz NS, Campbell F, Feltmate CM, et al. Evidence for lineage continuity between early serous proliferations (ESPs) in the Fallopian tube and disseminated high-grade serous carcinomas. J Pathol 2018;246:344–51.
15. Labidi-Galy SI, Papp E, Hallberg D, Niknafs N, Adleff V, Noe M, et al. High grade serous ovarian carcinomas originate in the fallopian tube. Nat Commun 2017;8:1093.
16. Rabban JT, Garg K, Crawford B, Chen L, Zaloudek CJ. Early detection of high-grade tubal serous carcinoma in women at low risk for hereditary breast and ovarian cancer syndrome by systematic examination of fallopian tubes incidentally removed during benign surgery. Am J Surg Pathol 2014;38:729–42.
17. Mahe E, Tang S, Deb P, Sur M, Lytwyn A, Daya D. Do deeper sections increase the frequency of detection of serous tubal intraepithelial carcinoma (STIC) in the 'sectioning and extensively examining the FIMbriated end' (SEE-FIM) protocol? Int J Gynecol Pathol 2013;32:353–7.
18. Soong T, Kolin D, Teschan N, Crum C. Back to the future? The fallopian tube, precursor escape and a dualistic model of high-grade serous carcinogenesis. Cancers 2018;10:468.
19. Cancer Genome Atlas Research Network. Integrated genomic analyses of ovarian carcinoma Nature 2011;474:609–15.
20. Macintyre G, Goranova TE, De Silva D, Ennis D, Piskorz AM, Eldridge M, et al. Copy number signatures and mutational processes in ovarian carcinoma. Nat Genet 2018;50:1262–70.
21. Wang YK, Bashashati A, Anglesio MS, Cochrane DR, Grewal DS, Ha G, et al. Genomic consequences of aberrant DNA repair mechanisms stratify ovarian cancer histotypes. Nat Genet 2017;49:856–65.
22. Gorringe KL, George J, Anglesio MS, Ramakrishna M, Etemadmoghadam D, Cowin P, et al. Copy number analysis identifies novel interactions between genomic loci in ovarian cancer. PLoS One 2010;5:e11408.
23. Kamieniak MM, Muñoz-Repeto I, Rico D, Osorio A, Urioste M, García-Donas J, et al. DNA copy number profiling reveals extensive genomic loss in

hereditary BRCA1 and BRCA2 ovarian carcinomas. Br J Cancer 2013;108: 1732–42.
24. Weber J, Rad R. Engineering CRISPR mouse models of cancer. Curr Opin Genet Dev 2019;54:88–96.
25. Shrock E, Güell M. CRISPR in animals and animal models. Prog Mol Biol Transl Sci 2017;152:95–114.
26. Bardeesy N, Sinha M, Hezel AF, Signoretti S, Hathaway NA, Sharpless NE, et al. Loss of the Lkb1 tumour suppressor provokes intestinal polyposis but resistance to transformation. Nature 2002;419:162–7.
27. Madisen L, Zwingman TA, Sunkin SM, Oh SW, Zariwala HA, Gu H, et al. A robust and high-throughput Cre reporting and characterization system for the whole mouse brain. Nat Neurosci 2010;13:133–40.
28. Takahashi G, Gurumurthy CB, Wada K, MH. GONAD: Genome-editing via O viductal nucleic acids delivery system : a novel microinjection independent genome engineering method in mice. Sci Rep 2015;5:11406.
29. Chazaud C, Yamanaka Y, Pawson T, Rossant J. Early lineage segregation between epiblast and primitive endoderm in mouse blastocysts through the Grb2-MAPK pathway. Dev Cell 2006;10:615–24.
30. Park J, Lim K, Kim JS, Bae S. Cas-analyzer: an online tool for assessing genome editing results using NGS data. Bioinformatics 2017;33:286–8.
31. Jiang H, Lei R, Ding SW, Zhu S. Skewer: a fast and accurate adapter trimmer for next-generation sequencing paired-end reads. BMC Bioinformatics 2014;15:182.
32. Li H, Durbin R. Fast and accurate short read alignment with Burrows-Wheeler transform Bioinformatics 2009;25:1754–60.
33. Talevich E, Shain AH, Botton T, Bastian BC. CNVkit: genome-wide copy number detection and visualization from targeted DNA sequencing. PLoS Comput Biol 2016;12:1004873.
34. Butler A, Hoffman P, Smibert P, Papalexi E, Satija R. Integrating single-cell transcriptomic data across different conditions, technologies, and species. Nat Biotechnol 2018;36:411–20.
35. Tickle T, Tirosh I, Georgescu C, Brown M, Haas B. inferCNV of the Trinity CTAT Project. Cambridge, MA: Klarman Cell Observatory, Broad Institute of MIT and Harvard; 2019. Available from: https://github.com/broadinstitute/inferCNV.
36. Shackelford DB, Shaw RJ. The LKB1 – AMPK pathway : metabolism and growth control in tumour suppression. Nat Rev Cancer 2009;9:563–75.
37. Shorning BY, Clarke AR. Energy sensing and cancer: LKB1 function and lessons learnt from Peutz-Jeghers syndrome. Semin Cell Dev Biol 2016;52:21–9.
38. Krawchuk D, Anani S, Honma-Yamanaka N, Polito S, Shafik M, Yamanaka Y. Loss of LKB1 leads to impaired epithelial integrity and cell extrusion in the early mouse embryo. J Cell Sci 2015;128:1011–22.
39. Kipps E, Tan DSP, Kaye SB. Meeting the challenge of ascites in ovarian cancer: New avenues for therapy and research. Nat Rev Cancer 2013;13:273–82.
40. Lengyel E. Ovarian cancer development and metastasis. Am J Pathol 2010;177: 1053–64.
41. Bobbs AS, Cole JM, Dahl KDC. Emerging and evolving ovarian cancer animal models Cancer Growth Metastasis 2015;8:29–36.
42. Eng KH, Morrell K, Starbuck K, Spring-Robinson C, Khan A, Cleason D, et al. Gynecologic Oncology Prognostic value of miliary versus non-miliary sub-staging in advanced ovarian cancer. Gynecol Oncol 2017;146:52–7.
43. Auer K, Bachmayr-Heyda A, Aust S, Sukhbaatar N, Reiner AT, Grimm C, et al. Peritoneal tumor spread in serous ovarian cancer-epithelial mesenchymal status and outcome Oncotarget 2015;6:17261–75.
44. Laury AR, Perets R, Piao H, Krane JF, Barletta JA, French C, et al. A comprehensive analysis of PAX8 expression in human epithelial tumors. Am J Surg Pathol 2011;35:816–26.
45. Zhai Y, Wu R, Kuick R, Sessine MS, Schulman S, Green M, et al. High-grade serous carcinomas arise in the mouse oviduct via defects linked to the human disease. J Pathol 2017;243:16–25.
46. Rouet P, Smih F, Jasin M. Introduction of double-strand breaks into the genome of mouse cells by expression of a rare-cutting endonuclease. Mol Cell Biol 1994; 14:8096–106.
47. Gaj T, Gersbach CA, Barbas CF. ZFN, TALEN, and CRISPR/Cas-based methods for genome engineering. Trends Biotechnol 2013;31:397–405.
48. Mehra K, Mehrad M, Ning G, Drapkin R, McKeon FD, Xian W, et al. STICS, SCOUTs and p53 signatures;a new language for pelvic serous carcinogenesis. Front Biosci 2011;3:625–34.
49. Crum CP, McKeon FD, Xian W. The oviduct and ovarian cancer: causality, clinical implications and 'targeted prevention. Clin Obstet Gynecol 2012;55: 24–35.
50. Tanwar PS, Mohapatra G, Chiang S, Engler DA, Zhang L, Kaneko-Tarui T, et al. Loss of LKB1 and PTEN tumor suppressor genes in the ovarian surface epithelium induces papillary serous ovarian cancer. Carcinogenesis 2014;35: 546–53.
51. Ford CE, Werner B, Hacker NF, Warton K. The untapped potential of ascites in ovarian cancer research and treatment. Br J Cancer 2020;123:9–16.
52. Schelker M, Feau S, Du J, Ranu N, Klipp E, MacBeath G, et al. Estimation of immune cell content in tumour tissue using single-cell RNA-seq data. Nat Commun 2017;8:2032.
53. Izar B, Tirosh I, Stover EH, Wakiro I, Cuoco MS, Alter I, et al. A single-cell landscape of high-grade serous ovarian cancer. Nat Med 2020;26:1271–9.
54. Matulonis UA, Sood AK, Fallowfield L, Howitt BE, Sehouli J, Karlan BY. Ovarian cancer. Nat Rev Dis Prim 2016;2:16061.
55. Karnezis AN, Cho KR, Gilks CB, Pearce CL, Huntsman DG. The disparate origins of ovarian cancers: Pathogenesis and prevention strategies. Nat Rev Cancer 2017;17:65–74.
56. Mueller S, Engleitner T, Maresch R, Zukowska M, Lange S, Kaltenbacher T, et al. Evolutionary routes and KRAS dosage define pancreatic cancer phenotypes. Nature 2018;554:62–8.
57. Reeves MQ, Kandyba E, Harris S, Del Rosario R, Balmain A. Multicolour lineage tracing reveals clonal dynamics of squamous carcinoma evolution from initiation to metastasis. Nat Cell Biol 2018;20:699–709.
58. Snippert HJ, van der Flier LG, Sato T, van Es JH, van den Born M, Kroon-Veenboer C, et al. Intestinal crypt homeostasis results from neutral competition between symmetrically dividing Lgr5 stem cells. Cell 2010;143:134–44.
59. Mort RL, Ford MJ, Sakaue-Sawano A, Lindstrom NO, Casadio A, Douglas AT, et al. Fucci2a: a bicistronic cell cycle reporter that allows Cre mediated tissue specific expression in mice. Cell Cycle 2014;13:2681–96.
60. Ford MJ, Yeyati PL, Mali GR, Keighren MA, Waddell SH, Mjoseng HK, et al. A Cell/Cilia cycle biosensor for single-cell kinetics reveals persistence of cilia after G1/S transition is a general property in cells and mice. Dev Cell 2018;47:509–23.
61. Aoyama N, Miyoshi H, Miyachi H, Sonoshita M, Okabe M, Taketo MM. Transgenic mice that accept Luciferase- or GFP-expressing syngeneic tumor cells at high efficiencies. Genes Cells 2018;23:580–9.
62. Yemelyanova AV, Cosin JA, Bidus MA, Boice CR, Seidman JD. Pathology of stage I versus stage III ovarian carcinoma with implications for pathogenesis and screening. Int J Gynecol Cancer 2008;18:465–9.
63. Kurman RF, Shih IM. The origin and pathogenesis of epithelial ovarian cancer: a proposed unifying theory. Am J Surg Pathol 2010;34:433–43.
64. Piek JMJ, Kenemans P, Verheijen RHM. Intraperitoneal serous adenocarcinoma: a critical appraisal of three hypotheses on its cause. Am J Obstet Gynecol 2004; 191:718–32.
65. Kim J, Park EY, Kim O, Schilder JM, Coffey DM, Cho CH, et al. Cell origins of high-grade serous ovarian cancer. Cancers 2018;10:433.
66. Torres D, Kumar A, Wallace SK, Bakkum-Gamez JN, Konecny GE, Weaver AL, et al. Intraperitoneal disease dissemination patterns are associated with residual disease, extent of surgery, and molecular subtypes in advanced ovarian cancer. Gynecol Oncol 2017;147:503–8.
67. Torres D, Wang C, Kumar A, Bakkum-Gamez JN, Weaver AL, McGree ME, et al. Factors that influence survival in high-grade serous ovarian cancer: a complex relationship between molecular subtype, disease dissemination, and operability. Gynecol Oncol 2018;150:227–32.